

Banner appropriate to article type will appear here in typeset article

Three-dimensional soft streaming

Songyuan Cui¹, Yashraj Bhosale¹, and Mattia Gazzola^{1,2,3,†}

¹Mechanical Sciences and Engineering, University of Illinois at Urbana-Champaign, Urbana, IL 61801, USA

²National Center for Supercomputing Applications, University of Illinois at Urbana-Champaign, Urbana, IL 61801, USA

³Carl R. Woese Institute for Genomic Biology, University of Illinois at Urbana-Champaign, Urbana, IL 61801, USA

(Received xx; revised xx; accepted xx)

Viscous streaming is an efficient rectification mechanism to exploit flow inertia at small scales for fluid and particle manipulation. It typically entails a fluid vibrating around an immersed solid feature that, by concentrating stresses, modulates the emergence of steady flows of useful topology. Motivated by its relevance in biological and artificial settings characterized by soft materials, recent studies have theoretically elucidated, in two dimensions, the impact of body elasticity on streaming flows. Here, we generalize those findings to three dimensions, via the minimal case of an immersed soft sphere. We first improve existing solutions for the rigid sphere limit, by considering previously unaccounted terms. We then enable body compliance, exposing a three-dimensional, elastic streaming process available even in Stokes flows. Such effect, consistent with two-dimensional analyses but analytically distinct, is validated against direct numerical simulations and shown to translate to bodies of complex geometry and topology, paving the way for advanced forms of flow control.

Key words: viscous streaming, microfluidics, elasticity, flow–structure interaction

1. Introduction

This study investigates the effects of body elasticity on three-dimensional viscous streaming. Viscous streaming, an inertial phenomenon, refers to the steady, rectified flows that emerge when a fluid oscillates around a localized microfeature. Given its ability to remodel surrounding flows over short time and length scales, streaming has found application in multiple aspects of microfluidics, from particle manipulation (Lutz *et al.* 2003, 2005; Marmottant & Hilgenfeldt 2004; Lutz *et al.* 2006; Wang *et al.* 2011; Chong *et al.* 2013; Chen & Lee 2014; Klotsa *et al.* 2015; Thameem *et al.* 2017; Pommella *et al.* 2021) and chemical mixing (Liu *et al.* 2002; Lutz *et al.* 2003, 2005; Ahmed *et al.* 2009) to vesicle transport and lysis (Marmottant & Hilgenfeldt 2003, 2004). Recently, the use of multi-curvature streaming bodies has expanded the ability to manipulate flows, leading to compact,

† Email address for correspondence: mgazzola@illinois.edu

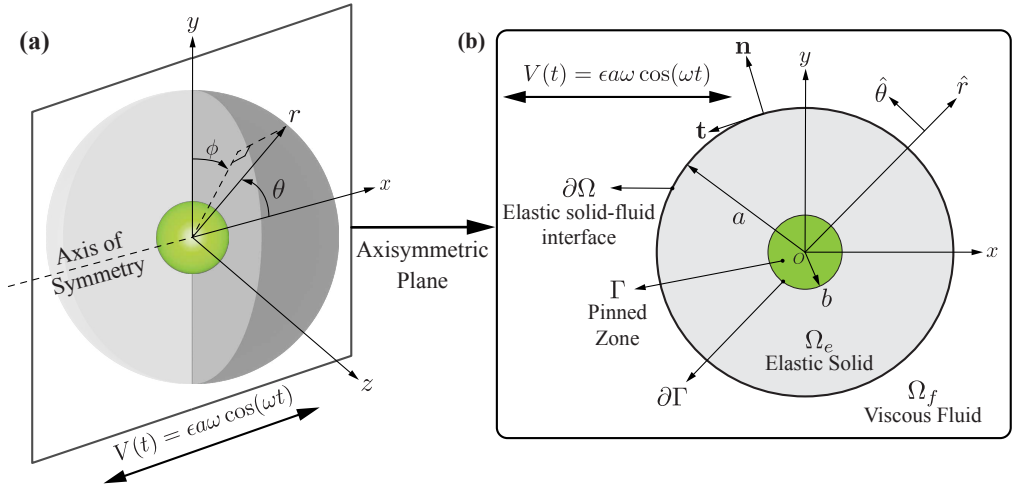


Figure 1: Problem setup. (a) 3D Elastic solid sphere Ω_e of radius a with a rigid inclusion (pinned zone Γ of radius b), immersed in viscous fluid Ω_f . In this study, we deploy a spherical coordinate system where (r, θ, ϕ) are the radial, polar, and azimuthal coordinates. The sphere is exposed to an oscillatory flow with far-field velocity $V(t) = \epsilon a \omega \cos(\omega t)$ in the x direction, along the axis of symmetry. (b) 2D axisymmetric cross-section of the elastic sphere.

robust, and tunable devices for filtering and separating both synthetic and biological particles (Parthasarathy *et al.* 2019; Bhosale *et al.* 2020; Chan *et al.* 2022; Bhosale *et al.* 2022b). More recently yet, motivated by medical and biological applications, the effect of body compliance has been considered (Pande *et al.* 2023; Anand & Christov 2020), with one of the studies yielding a first two-dimensional streaming theory for soft cylinders (Bhosale *et al.* 2022a). Its major outcome is encapsulated in the relation

$$\langle \psi_1 \rangle = \sin 2\theta [\Theta(r) + \Lambda(r)] \quad (1.1)$$

where $\langle \psi_1 \rangle$ is the time-averaged Stokes streamfunction, r and θ are the radial and polar coordinates in the cylindrical system. This relation reveals an additional streaming process $\Lambda(r)$, purely induced by body elasticity, that is available even in Stokes flows where rigid-body streaming $\Theta(r)$ cannot exist (Holtmark *et al.* 1954). Elasticity modulation has then been shown to achieve streaming configurations similar to rigid bodies, but at significantly lower frequencies. This frequency reduction has relevant implications, as it renders viscous streaming accessible within the limits of biological actuation.

In this work, we extend this understanding to three dimensions by examining the minimal case of an oscillating, soft sphere. We first present an improved theoretical solution for the rigid sphere case by augmenting Lane (1955)'s derivation with a previously unaccounted term related to vortex stretching. Our formulation is shown to significantly enhance quantitative agreement with direct numerical simulations and experiments. Next, within the same theoretical framework, we consider body elasticity and seek a modified streaming solution dependent on material compliance. We recover an independent elastic modification term, similar in nature to the above two-dimensional result but analytically distinct. We then demonstrate the accuracy of our theory against direct numerical simulations, and show how observed elasticity effects may translate to bodies of complex geometry and topology, further expanding the potential utility of soft streaming.

2. Problem setup and governing equations

We derive the streaming solution by considering the setup shown in Fig. 1, where a 3D viscoelastic solid sphere Ω_e of radius a is immersed in a viscous fluid Ω_f . The fluid oscillates with velocity $V(t) = \epsilon a \omega \cos \omega t$, where ϵ , ω and t represent the non-dimensional amplitude, angular frequency, and time. Following our previous setup for a soft 2D cylinder (Bhosale *et al.* 2022a), we kinematically enforce zero strain and velocity near the sphere's center by 'pinning' the sphere with a rigid inclusion Γ of radius $b < a$, the boundary of which is denoted by $\partial\Gamma$. We further denote by $\partial\Omega$ the boundary between the elastic solid and the viscous fluid.

Both fluid and solid are assumed to be isotropic and incompressible, where the fluid is Newtonian with kinematic viscosity ν_f and density ρ_f , and the solid follows the Kelvin-Voigt viscoelastic model. Characteristic of soft biological materials (Bower 2009), elastic stresses within the solid are modeled via neo-Hookean hyperelasticity with shear modulus G , kinematic viscosity ν_e , and density ρ_e . However, we will later show that the choice of hyperelastic or viscoelastic model does not affect the theory.

The dynamics in the fluid and solid phases are governed by the incompressible Cauchy momentum equations, non-dimensionalized using the characteristic scales of velocity $V = \epsilon a \omega$, length $L = a$, time $T = 1/\omega$, and hydrostatic pressure $P = \mu_f V/L = \mu_f \epsilon \omega$

$$\begin{aligned} \text{Incomp. } & \left\{ \nabla \cdot \mathbf{v} = 0, \mathbf{x} \in \Omega_f \cup \Omega_e \right. \\ \text{Fluid } & \left\{ \frac{\partial \mathbf{v}}{\partial t} + \epsilon (\mathbf{v} \cdot \nabla) \mathbf{v} = \frac{1}{M^2} (-\nabla p + \nabla^2 \mathbf{v}), \mathbf{x} \in \Omega_f \right. \\ \text{Solid } & \left\{ \alpha \text{Cau} \left(\frac{\partial \mathbf{v}}{\partial t} + \epsilon (\mathbf{v} \cdot \nabla) \mathbf{v} \right) = \frac{\text{Cau}}{M^2} (-\nabla p + \beta \nabla^2 \mathbf{v}) + \nabla \cdot (\mathbf{F} \mathbf{F}^T)', \mathbf{x} \in \Omega_e, \right. \end{aligned} \quad (2.1)$$

where \mathbf{v} and p are the velocity and pressure fields, and \mathbf{F} is the deformation gradient tensor, defined as $\mathbf{F} = \mathbf{I} + \nabla \mathbf{u}$, where \mathbf{I} is the identity, $\mathbf{u} = \mathbf{x} - \mathbf{X}$ is the material displacement field, and \mathbf{x} , \mathbf{X} are the position of a material point after deformation and at rest, respectively. The prime symbol ' on a tensor denotes its deviatoric. The key non-dimensional parameters within this system are the scaled oscillation amplitude ϵ , Womersley number $M = a \sqrt{\rho_f \omega / \mu_f}$, Cauchy number $\text{Cau} = \epsilon \rho_f a^2 \omega^2 / G$, density ratio $\alpha = \rho_e / \rho_f$, and viscosity ratio $\beta = \mu_e / \mu_f$. Physically, the Womersley number (M) represents the ratio of inertial to viscous forces, and the Cauchy number (Cau) represents the ratio of inertial to elastic forces. Therefore, a higher M corresponds to stronger dominance of inertia in the fluid environment, and higher Cau values correspond to increasingly soft bodies. We then impose a set of boundary conditions upon the governing equations, consistent with Lane (1955)

$$\text{Pinned zone } \left\{ \mathbf{u} = 0, \mathbf{v} = 0, \mathbf{x} \in \Gamma \right. \quad (2.2)$$

$$\text{Interface velocity } \left\{ \mathbf{v}_e = \mathbf{v}_f, \mathbf{x} \in \partial\Omega \right. \quad (2.3)$$

$$\text{Interface stresses } \left\{ \begin{aligned} \sigma_f &= -p \mathbf{I} + (\nabla \mathbf{v} + \nabla \mathbf{v}^T), \mathbf{x} \in \Omega_f \\ \sigma_e &= -p \mathbf{I} + \beta (\nabla \mathbf{v} + \nabla \mathbf{v}^T) + \frac{M^2}{\text{Cau}} (\mathbf{F} \mathbf{F}^T)', \mathbf{x} \in \Omega_e, \\ \mathbf{n} \cdot \sigma_e \cdot \mathbf{n} &= \mathbf{n} \cdot \sigma_f \cdot \mathbf{n}, \mathbf{x} \in \partial\Omega \\ \mathbf{n} \cdot \sigma_e \cdot \mathbf{t} &= \mathbf{n} \cdot \sigma_f \cdot \mathbf{t}, \mathbf{x} \in \partial\Omega \end{aligned} \right. \quad (2.4)$$

$$\text{Far-field } \left\{ \mathbf{v}(|\mathbf{x}| \rightarrow \infty) = \cos t \hat{\mathbf{i}}, \mathbf{x} \in \Omega_f, \right. \quad (2.5)$$

where Eq. (2.2) is the pinned-zone rigidity constraint, Eq. (2.3) is the no-slip boundary condition between and solid and fluid phases, Eq. (2.4) dictates stress continuity, and Eq. (2.5)

is the far-field flow velocity. We use subscripts e and f to denote elastic and fluid phases, respectively, wherever ambiguity may arise. Next, we identify ranges of relevant parameters and solve Eq. (2.1) via perturbation theory.

3. Perturbation series solution

In viscous streaming applications, typically we have small non-dimensional oscillation amplitudes $\epsilon \ll 1$ (Wang 1965; Bertelsen *et al.* 1973; Lutz *et al.* 2005), density ratio α and viscosity ratio β of $\mathcal{O}(1)$, and Womersley number $M \geq \mathcal{O}(1)$ (Marmottant & Hilgenfeldt 2004; Lutz *et al.* 2006). For the Cauchy number Cau , we apply the same treatment as Bhosale *et al.* (2022a), where we use $\text{Cau} = 0$ for a rigid body and $\text{Cau} = \kappa\epsilon$ with $\kappa = \mathcal{O}(1)$ for elastic bodies. The latter assumption implies that $\text{Cau} \ll 1$, which physically means that the body is weakly elastic. We make this assumption for two reasons. First, we choose Cau to be small to simplify the treatment of hyperelastic materials, whose non-linearities become mathematically challenging for $\text{Cau} \geq \mathcal{O}(1)$. Second, matching Cau with ϵ simplifies the asymptotic expansion, while preserving the practical generality of the results (for details, see supplementary material §2 of Bhosale *et al.* (2022a)).

We then seek a perturbation series solution of Eqs. (2.1) by asymptotically expanding all relevant fields in powers of ϵ . Our derivation closely follows the approach taken by (Bhosale *et al.* 2022a) for 2D elastic cylinders, while augmenting it to encompass 3D settings. Then, the zeroth order solution reduces to a rigid sphere in a purely oscillatory flow governed by the unsteady Stokes equation (Lane 1955). The first order solution is subsequently derived in two stages. First, we obtain the deformation of the elastic body resulting from the flow field at zeroth order. Second, we incorporate the elastic feedback into the streaming solution by using the obtained body deformations as boundary conditions for the flow at $\mathcal{O}(\epsilon)$. The steps are outlined below, with details listed in the supplementary material.

We start by perturbing to $\mathcal{O}(\epsilon)$ all physical quantities q , which include \mathbf{v} , \mathbf{u} , p , Ω , \mathbf{n} , \mathbf{t} , as

$$q \sim q_0 + \epsilon q_1 + \mathcal{O}(\epsilon^2) \quad (3.1)$$

and substitute them into the governing equations Eqs. (2.1) and boundary conditions Eqs. (2.2)–(2.5). Steps are explicitly reported in the supplementary material (Eq.1.17–1.26), where subscripts (0, 1, ...) refer to the solution order. Next, we adopt the geometrically convenient spherical coordinate system (r, θ, ϕ) , with radial coordinate r , polar angle θ , azimuthal angle ϕ , and origin at the center of the sphere. The horizontal axis direction \mathbf{i} corresponds to $\theta = 0$.

3.1. Zeroth order $\mathcal{O}(1)$ solution

The governing equations and boundary conditions in the solid phase at zeroth order $\mathcal{O}(1)$ simplify to

$$\nabla \cdot ((\mathbf{I} + \nabla \mathbf{u}_0)(\mathbf{I} + \nabla \mathbf{u}_0)^T)' = 0, \quad r \leq 1; \quad \mathbf{u}_0|_{r=\zeta} = 0 \quad (3.2)$$

where $\zeta = b/a$ is the non-dimensional radius of the pinned zone. Since at this order $\text{Cau} = \kappa\epsilon = 0$, the solution of Eq. (3.2) physically corresponds to a fixed, rigid sphere with

$$\partial\Omega_0 = r = 1; \quad \mathbf{u}_0 = 0, \quad \mathbf{v}_0 = \frac{\partial \mathbf{u}_0}{\partial t} = 0, \quad r \leq 1. \quad (3.3)$$

Thus the fluid phase governing equations and boundary conditions reduce to

$$M^2 \frac{\partial \nabla^2 \varphi_0}{\partial t} = \nabla^4 \varphi_0 \quad r \geq 1$$

$$v_{0,r}|_{r=1} = \frac{1}{r \sin \theta} \frac{\partial(\varphi_0 \sin \theta)}{\partial \theta} \Big|_{r=1} = 0; \quad v_{0,\theta}|_{r=1} = -\frac{1}{r} \frac{\partial(r\varphi_0)}{\partial r} \Big|_{r=1} = 0 \quad (3.4)$$

$$v_{0,r}|_{r \rightarrow \infty} = \cos \theta \cos t; \quad v_{0,\theta}|_{r \rightarrow \infty} = -\sin \theta \cos t,$$

where $\boldsymbol{\varphi} = \varphi \hat{\boldsymbol{\phi}}$ is the vector potential defined as $\boldsymbol{v} = \nabla \times \boldsymbol{\varphi}$, with $\hat{\boldsymbol{\phi}}$ being the unit vector in the azimuthal direction. We note that the bold font ∇^2 refers to the vector Laplacian operator, which is distinct from the scalar Laplacian operator in spherical coordinates. This system (Eqs. (3.3), (3.4)) defines a rigid sphere immersed in an oscillating unsteady Stokes flow, which has an exact analytical solution (Lane 1955)

$$\varphi_0 = -\frac{\sin \theta}{4} \left(3 \frac{h_1(mr)}{mh_0(m)} - r - \frac{h_2(m)}{r^2 h_0(m)} \right) e^{-it} + c.c., \quad r \geq 1 \quad (3.5)$$

where $i = \sqrt{-1}$, and $m = \sqrt{i}M$. Here, h_n and *c.c.* refer to the n^{th} order spherical Hankel function of the first kind and complex conjugate, respectively. As observed in Lane (1955), the zeroth order vector potential field $\boldsymbol{\varphi}_0$ in the fluid phase is purely oscillatory in time, and thus no steady streaming appears at this order. Moreover, the flow at $O(1)$ is unaffected by elasticity.

3.2. First order $O(\epsilon)$ solution

We then proceed to the next order approximation $O(\epsilon)$, where we expect time-independent steady streaming to emerge (Lane 1955). At $O(\epsilon)$, the solid governing equations reduce (supplementary material, Eqs. 1.38-1.42, 1.49) to the homogeneous biharmonic equation

$$\nabla^4 \varphi_{e,1} = 0, \quad \boldsymbol{x} \in \Omega_e \quad (3.6)$$

where we have defined the strain function $\varphi_e = \varphi_e \hat{\boldsymbol{\phi}}$ similar to the fluid phase, so that the displacement field is $\boldsymbol{u} = \nabla \times \boldsymbol{\varphi}_e$. Equation (3.6) demonstrates how the specific choice of solid elasticity model used at $O(\epsilon)$ becomes irrelevant, since all nonlinear stress-strain responses drop out as a result of linearization (supplementary material, Eqs. 1.38–1.42). Equation (3.6) is complemented by the Dirichlet boundary conditions at the pinned zone interface

$$u_{1,r} = \frac{1}{r \sin \theta} \frac{\partial(\varphi_{e,1} \sin \theta)}{\partial \theta} \Big|_{r=\zeta} = 0; \quad u_{1,\theta} = -\frac{1}{r} \frac{\partial(r\varphi_{e,1})}{\partial r} \Big|_{r=\zeta} = 0. \quad (3.7)$$

Additionally, in accordance with Eq. (2.4), the $O(1)$ flow solution exerts interfacial stresses on the solid, which at $O(\epsilon)$ is no longer rigid but instead deformable. This results in the following boundary conditions for the radial and tangential stresses at the interface $\partial\Omega_0$

$$\frac{M^2}{\kappa} \frac{\partial u_{1,r}}{\partial r} \Big|_{r=1} = \frac{\partial v_{0,r}}{\partial r} \Big|_{r=1}$$

$$\frac{M^2}{\kappa} \left(\frac{1}{r} \frac{\partial u_{1,r}}{\partial \theta} + \frac{\partial u_{1,\theta}}{\partial r} - \frac{u_{1,\theta}}{r} \right) \Big|_{r=1} = \left(\frac{1}{r} \frac{\partial v_{0,r}}{\partial \theta} + \frac{\partial v_{0,\theta}}{\partial r} - \frac{v_{0,\theta}}{r} \right) \Big|_{r=1}, \quad (3.8)$$

where the LHS corresponds to the elastic stresses in the solid phase ($\frac{M^2}{\text{Cau}} (\boldsymbol{F}\boldsymbol{F}^T)'$, Eq. (2.4)) and the RHS to the viscous stresses in the fluid phase ($\nabla \boldsymbol{v} + \nabla \boldsymbol{v}^T$, Eq. (2.4)), both evaluated at the zeroth order interface $r = 1$. The pressure term ($-p\boldsymbol{I}$, Eq. (2.4)) cancels out due to pressure continuity at the interface, hence its absence in Eq. (3.8) (supplementary material,

Eq. 1.31). We point out that the use of $r = 1$ in Eq. (3.8) is consistent despite the fact that the solid interface deforms at this order. Indeed, as demonstrated in Bhosale *et al.* (2022a) and supplementary material Eqs. 1.44–1.46, errors associated with the $r = 1$ approximation all appear at the higher order $O(\epsilon^2)$ and thus do not affect our solution. In addition, we note that the viscous stress term ($\beta(\nabla\mathbf{v} + \nabla\mathbf{v}^T)$, Eq. (2.4)) is also of higher order $O(\epsilon^2)$ and thus absent in Eq. (3.8), implying that the specific choice of viscosity model is irrelevant at $O(\epsilon)$. Next, we use the $O(1)$ flow velocity at the interface, Eqs. (3.4) and (3.5), to directly evaluate the RHS of Eq. (3.8)

$$\begin{aligned} \left. \frac{\partial v_{0,r}}{\partial r} \right|_{r=1} &= 0 \\ \left(\frac{1}{r} \frac{\partial v_{0,r}}{\partial \theta} + \frac{\partial v_{0,\theta}}{\partial r} - \frac{v_{0,\theta}}{r} \right) \Big|_{r=1} &= \sin \theta F(m) e^{-it} + c.c. \end{aligned} \quad (3.9)$$

with

$$F(m) = -\frac{3mh_1(m)}{4h_0(m)}. \quad (3.10)$$

With the boundary conditions Eqs. (3.7) – (3.10) resolved, the homogeneous biharmonic Eq. (3.6) can be solved exactly to obtain the $O(\epsilon)$ solid strain function

$$\varphi_{e,1} = \frac{\kappa}{M^2} \sin \theta \left(c_1 r + \frac{c_2}{r^2} + c_3 r^3 + c_4 \right) F(m) e^{-it} + c.c., \quad (3.11)$$

where the exact expressions for c_1, c_2, c_3, c_4 (functions of ζ) are reported in the supplementary material (Eq. 1.56). The $O(\epsilon)$ solid displacement field \mathbf{u}_1 , both in the bulk Ω_e and at the boundary $\partial\Omega$, can then be directly obtained from Eq. (3.11). This, in turn, kinematically affects the flow at $O(\epsilon)$ via the interfacial boundary conditions, as we will see.

The flow governing equation at $O(\epsilon)$, in vector potential form, reads

$$M^2 \frac{\partial \nabla^2 \boldsymbol{\varphi}_1}{\partial t} + M^2 \left((\mathbf{v}_0 \cdot \nabla) \nabla^2 \boldsymbol{\varphi}_0 \right) - M^2 \left((\nabla^2 \boldsymbol{\varphi}_0 \cdot \nabla) \mathbf{v}_0 \right) = \nabla^4 \boldsymbol{\varphi}_1, \quad r \geq 1. \quad (3.12)$$

We note that the term $M^2(\nabla^2 \boldsymbol{\varphi}_0 \cdot \nabla) \mathbf{v}_0$ in Eq. (3.12), which corresponds to vortex stretching, is absent in the rigid sphere streaming derivation of Lane (1955). By considering this unaccounted term, our work improves upon the existing theory, as demonstrated in Section 4.

Next, since we are interested in steady streaming, we consider the time-averaged form of Eq. (3.12)

$$\nabla^4 \langle \boldsymbol{\varphi}_1 \rangle = M^2 \underbrace{\langle (\mathbf{v}_0 \cdot \nabla) \nabla^2 \boldsymbol{\varphi}_0 - (\nabla^2 \boldsymbol{\varphi}_0 \cdot \nabla) \mathbf{v}_0 \rangle}_{\text{RHS}}, \quad r \geq 1, \quad (3.13)$$

where we substitute Eq. (3.5) into the RHS to yield

$$\begin{aligned} \nabla^4 \langle \boldsymbol{\varphi}_1 \rangle &= \sin 2\theta \rho(r) \hat{\boldsymbol{\phi}}, \quad r \geq 1, \\ \rho(r) &= \frac{1}{16r^4} \left(r^3 J^{(3)} + r^2 J^{(2)} - 6r J^{(1)} + 6J \right) J^* + c.c. \\ J(r) &= 3 \frac{h_1(mr)}{mh_0(m)} - r - \frac{h_2(m)}{r^2 h_0(m)}. \end{aligned} \quad (3.14)$$

Here, J is the radially dependent term of Eq. (3.5), with $J^{(n)}$ and J^* being its n^{th} derivative and complex conjugate, respectively. Solving this inhomogeneous biharmonic equation requires four independent boundary conditions. The first two are the radial and tangential, time-

averaged, far-field velocity

$$\frac{1}{r \sin \theta} \frac{\partial(\langle \varphi_1 \rangle \sin \theta)}{\partial \theta} \Big|_{r \rightarrow \infty} = \frac{1}{r} \frac{\partial(r \langle \varphi_1 \rangle)}{\partial r} \Big|_{r \rightarrow \infty} = 0. \quad (3.15)$$

Next, we recall the no-slip boundary condition of Eq. (2.3) that needs to be enforced at the $O(\epsilon)$ accurate solid–fluid interface

$$\mathbf{v}_e|_{\partial\Omega} = \mathbf{v}_e|_{r=1+\epsilon u_{1,r}} + O(\epsilon^2) = \mathbf{v}_f|_{\partial\Omega} = \mathbf{v}_f|_{r=1+\epsilon u_{1,r}} + O(\epsilon^2). \quad (3.16)$$

We note that the sphere interface at $O(\epsilon)$ deforms as $r' = 1 + \epsilon u_{1,r}$, where $u_{1,r}$ is the radial component of the $O(\epsilon)$ accurate displacement field obtained by taking the curl of the strain function $\mathbf{u}_1 = \nabla \times \boldsymbol{\varphi}_{e,1}$. Similar to Bhosale *et al.* (2022a), we enforce the no-slip boundary condition in Eq. (3.16) by deploying the technique presented in Longuet-Higgins (1998), where $\mathbf{v}_f|_{r=r'}$ is Taylor expanded about $r = 1$ (supplementary material, Eqs. 1.64–1.66)

$$\mathbf{v}_f|_{r=1+\epsilon u_{1,r}} = \left(\mathbf{v}_{f,1} + \epsilon \frac{\partial \mathbf{v}_{f,0}}{\partial r} u_{1,r} \right) \Big|_{r=1} + O(\epsilon^2). \quad (3.17)$$

The boundary solid velocity $\mathbf{v}_e|_{r=1+\epsilon u_{1,r}}$ (LHS of Eq. (3.16)) can be instead computed to $O(\epsilon)$ accuracy as $\partial u_{1,r}/\partial t|_{r=1}$ (supplementary material, Eq. 1.63). We note that both $u_{1,r}$ and $\partial \mathbf{v}_{f,0}/\partial r$ are known from Eqs. (3.5) and (3.11). Thus, the $O(\epsilon)$ flow velocity $\mathbf{v}_{f,1}$ at $r = 1$, denoted by \mathbf{v}_1 henceforth, can be obtained by substituting Eq. (3.17) into Eq. (3.16) (supplementary material, Eqs. 1.62–1.67). Time averaging then yields the remaining two boundary conditions for Eq. (3.14)

$$\begin{aligned} \langle v_{1,r} \rangle \Big|_{r=1} &= \frac{1}{r \sin \theta} \frac{\partial(\langle \varphi_1 \rangle \sin \theta)}{\partial \theta} \Big|_{r=1} = 0 \\ \langle v_{1,\theta} \rangle \Big|_{r=1} &= -\frac{1}{r} \frac{\partial(r \langle \varphi_1 \rangle)}{\partial r} \Big|_{r=1} = -\frac{\kappa}{M^2} \sin 2\theta G_1(\zeta) F(m) F^*(m) \end{aligned} \quad (3.18)$$

with

$$G_1(\zeta) = \frac{(\zeta - 1)^2(4\zeta^2 + 7\zeta + 4)}{3\zeta(2\zeta^3 + 4\zeta^2 + 6\zeta + 3)}. \quad (3.19)$$

Equation (3.18) physically implies a rectified tangential slip velocity ($\langle v_{1,\theta} \rangle|_{r=1} \neq 0$) in the fluid phase at the zeroth-order fixed interface $r = 1$. This slip velocity captures the effect of body elastic deformation ($\langle v_{1,\theta} \rangle|_{r=1} = 0$ for rigid bodies) by equivalently modifying the fluid Reynolds stresses ($\sin 2\theta \rho(r)$ in Eq. (3.14)), thus impacting the resulting streaming flow. We further remark that, in contrast to rigid body streaming, such modification is accessible even in the Stokes limit as it is independent of the Navier-Stokes nonlinear inertial advection, a conclusion similarly drawn in our previous work on 2D soft cylinder streaming (Bhosale *et al.* 2022a). This phenomenon shares characteristics with the artificial mixed-mode streaming of pulsating bubbles (Longuet-Higgins 1998; Spelman & Lauga 2017), whereas the streaming process derived here arises spontaneously from the coupling between viscous fluid and elastic solid.

Given the steady flow of Eq. (3.14) and boundary conditions of Eqs. (3.15) and (3.18), the streaming solution can finally be written as

$$\langle \varphi_1 \rangle = \sin 2\theta [\Theta(r) + \Lambda(r)], \quad (3.20)$$

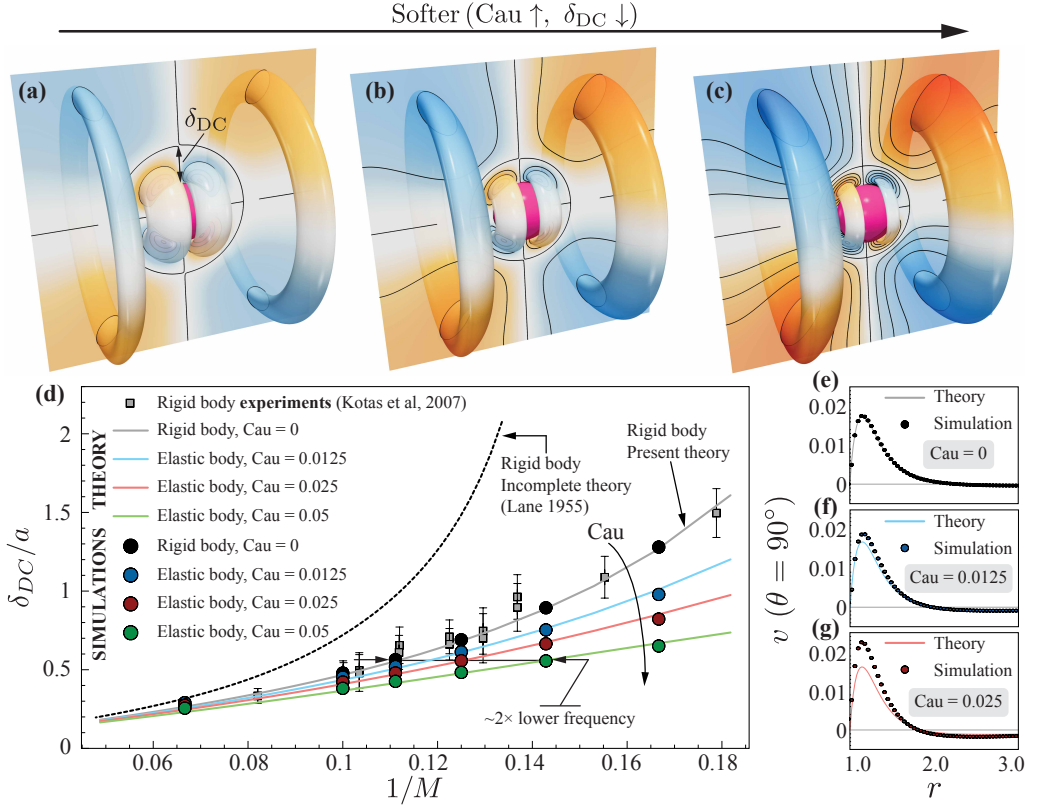


Figure 2: Elastic sphere and streaming flow response. (a-c) 3D time-averaged Lagrangian (i.e. Stokes-drift corrected, supplementary material §3) Stokes streamfunction depicting the streaming response at $M = 6$ with increasing softness Cau . (a) Rigid limit $\text{Cau} = 0$, (b) $\text{Cau} = 0.025$, and (c) $\text{Cau} = 0.05$. Note that blue/orange represent clockwise/counterclockwise rotating regions. The non-dimensional radius of the pinned zone is set at $\zeta = 0.4$ throughout the study, to maintain the tangential slip velocity magnitude (Eq. 3.18) at $O(1)$, consistent with the asymptotic analysis. Lowering the pinned zone radius rapidly increases the prefactor $G_1(\zeta)$ (Eq. 3.19), which results in a slip velocity much greater than $O(1)$, thereby weakening the asymptotic assumption. The opposite holds true for large ζ , rendering $\zeta = 0.4$ a robust compromise. The effect of pinned zone radius on streaming flow is detailed in Section §4 of the supplementary material. (d) Normalized DC layer thickness (δ_{DC}/a) vs. inverse Womersley number ($1/M$) from theory and simulations, for varying body elasticity Cau . Incomplete theory (dashed line) (Lane 1955) and experimental results (grey squares) (Kotas *et al.* 2007) in the rigidity limit are plotted for reference. We characterize streaming via the thickness of the DC layer, which refers to the innermost recirculation zone, for its utility in trapping, filtration and chemical mixing, and because of its robust nature. (e-g) Radial decay of velocity magnitude along $\theta = 90^\circ$ from theory and simulations at $M = 6$, with increasing softness Cau . (e) Rigid limit $\text{Cau} = 0$, (f) $\text{Cau} = 0.0125$, and (g) $\text{Cau} = 0.025$. Simulations are performed using a vortex-method based formulation (Gazzola *et al.* 2011; Bhosale *et al.* 2021, 2023) that solves the vorticity form of the Navier–Stokes equations in an axisymmetric cylindrical coordinate system. Within this framework, fluid and solid are modeled to be density matched ($\rho_f = \rho_e = 1$). The rigid sphere and pinned zone are modeled as Brinkman solids, and the elastic phase as a viscoelastic Kelvin–Voigt solid with shear modulus G . Soft body deformations are tracked using an inverse-map technique (Bhosale *et al.* 2021; Kamrin & Nave 2009; Kamrin *et al.* 2012). The far-field velocity is $V(t) = V_0 \cos \omega t$ with characteristic velocity $V_0 = \epsilon a \omega$, where $\epsilon = 0.1$, $a = 0.1$, and $\omega = 32\pi$. The fluid dynamic viscosity μ_f and elastic body’s shear modulus G are determined based on the Womersley number $M = a\sqrt{\rho_f \omega / \mu_f}$ and Cauchy number $\text{Cau} = \epsilon \rho_f a^2 \omega^2 / G$. Additional simulation parameters include: domain $[0, 1] \times [0, 0.5]$, uniform grid spacing $h = 1/1024$, Brinkman penalization factor $\lambda = 1e6$, mollification length $\epsilon_{moll} = 2h$, Courant–Friedrichs–Lewy number $\text{CFL} = 0.1$. For details on these parameters, refer to (Gazzola *et al.* 2011; Bhosale *et al.* 2021; Parthasarathy *et al.* 2022; Bhosale *et al.* 2023).

where $\Theta(r)$ is the rectified rigid-body solution

$$\begin{aligned} \Theta(r) = & -\frac{r^4}{70} \int_r^\infty \frac{\rho(\tau)}{\tau} d\tau + \frac{r^2}{30} \int_r^\infty \tau \rho(\tau) d\tau \\ & + \frac{1}{r} \left(\frac{1}{30} \int_1^r \tau^4 \rho(\tau) d\tau + \frac{1}{20} \int_1^\infty \frac{\rho(\tau)}{\tau} d\tau - \frac{1}{12} \int_1^\infty \tau \rho(\tau) d\tau \right) \\ & + \frac{1}{r^3} \left(-\frac{1}{70} \int_1^r \tau^6 \rho(\tau) d\tau - \frac{1}{28} \int_1^\infty \frac{\rho(\tau)}{\tau} d\tau + \frac{1}{20} \int_1^\infty \tau \rho(\tau) d\tau \right) \end{aligned} \quad (3.21)$$

and $\Lambda(r)$ is the new elastic modification

$$\Lambda(r) = 0.5 \frac{\kappa}{M^2} G_1(\zeta) F(m) F^*(m) \left(\frac{1}{r} - \frac{1}{r^3} \right) \quad (3.22)$$

with $G_1(\zeta)$ and $F(m)$ given in Eq. (3.19) and Eq. (3.10), respectively. We note that while Eq. (3.21) is of the same form as Lane (1955)'s solution, the explicit expression of $\rho(r)$ is different (Eq. 3.14) because of the vortex stretching term of Eq. (3.12). This concludes our theoretical analysis.

4. Numerical validation and extension to complex bodies

Next, we compare our theory against known experimental and analytical results in the rigidity limit (Kotas *et al.* 2007; Lane 1955), as well as direct numerical simulations performed using an axisymmetric vortex-method based formulation (Gazzola *et al.* 2012; Bhosale *et al.* 2021, 2023) (see also the caption of Fig. 2). The Stokes streamfunction pattern for a rigid sphere ($\text{Cau} = 0$) oscillating at $M \approx 6$ is shown in Fig. 2a. We highlight the two-fold symmetry on top of the axisymmetry, and the presence of a well-defined direct circulation (DC) layer of thickness δ_{DC} . This characteristic flow configuration, as well as the divergence of the DC layer thickness ($\delta_{DC} \rightarrow \infty$) with increasing $1/M$, is consistent with Lane (1955). This qualitative behavior is recovered by our theory at $\text{Cau} = 0$ (grey line in Fig. 2d), and by simulations (black dots in Fig. 2d). However, we note the significant quantitative difference between the results from Lane (1955) (black dashed line in Fig. 2d) and our simulations/theory, which are instead found to be in close agreement with experimental results (grey dots) by Kotas *et al.* (2007) (grey squares). The additional accuracy of our theory directly stems from including the vortex stretching term of Eq. (3.13), as previously discussed. Next, as we enable solid compliance ($\text{Cau} > 0$), we observe that the two-fold symmetry is preserved ($\sin 2\theta$ in Eq. (3.20)) while δ_{DC} contracts due to the elastic modification term $\Lambda \neq 0$, in agreement with numerical simulations across a range of Cau (Fig. 2(b-d)). These observations are consistent with our previous work on streaming for a 2D soft cylinder (Bhosale *et al.* 2022a), and thus a similar, intuitive explanation exists. The flow receives feedback deformation velocities on account of the deformable sphere surface, which acts as an additional source of inertia. Since the Womersley number (M) is the ratio between inertial and viscous forces, this is equivalent to rigid body streaming with a larger M , hence the decrease of DC layer thickness with increasing elasticity. This implies that an elastic body can access the streaming flow configurations of its rigid counterpart with significantly lower oscillation frequencies. Such frequency reduction is shown in Fig. 2d where, for example at $\text{Cau} = 0.05$, the same DC layer thickness is achieved at $\sim 2\times$ lower frequency. Similar to rigid objects, the δ_{DC} of a soft sphere still diverges with decreasing M , albeit at lower values, since the elastic modification $\Lambda(r)$ does not alter the asymptotic behavior of the rigid contribution $\Theta(r)$ (see supplementary material, Section 6 for details). We further note that as Cau increases and M decreases, the deviation between simulations and theory grows. This follows from the fact that as κ/M^2 in

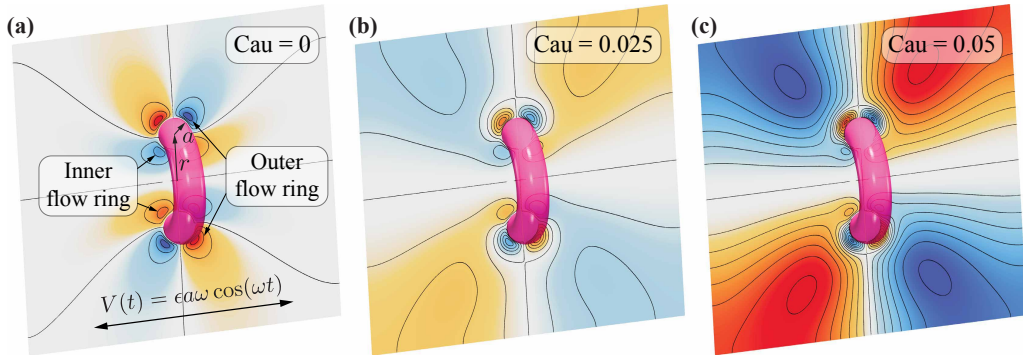


Figure 3: **Extension to complex bodies.** Here we consider compliance-induced streaming in a soft torus, a complex shape entailing multiple curvatures and distinct topology relative to the sphere. Numerically simulated time-averaged Eulerian flow topologies for a torus of core radius r and cross-sectional radius $a = r/3$, at $M \approx 4$, with varying body elasticity Cau . (a) Rigid limit $\text{Cau} = 0$, (b) $\text{Cau} = 0.025$, and (c) $\text{Cau} = 0.05$. The viscous fluid oscillates with velocity $V(t) = \epsilon a \omega \cos(\omega t)$. The torus is ‘pinned’ at the center of its circular cross-section by a rigid toroidal inclusion of radius $0.4a$. All other physical and simulation parameters are consistent with sphere streaming (see captions of Fig. 2 for details).

Eq. (3.18) increases, the tangential slip velocity assumed to be of $O(\epsilon)$ can exceed $O(1)$, eventually leading to the breakdown of the asymptotic analysis. We conclude our validation by showing close agreement between theoretical and simulated radially-varying, time-averaged velocities $\langle v \rangle$ at $\theta = 90^\circ$ (Fig. 2(e–g)). For a detailed analysis concerning the effect of inertia (M) and elasticity (Cau) on velocity magnitudes (flow strength), refer to Section 4 of the supplementary material.

Finally, we demonstrate how gained theoretical insights translate to 3D geometries characterized by multiple curvatures and distinct topology, illustrated here by means of a torus, a shape of interest due to its microfluidic properties (Chan *et al.* 2022) and recent bioengineered demonstrations (Dou *et al.* 2022). Figure 3a presents the streaming flow generated for a rigid torus immersed in an oscillatory flow field at $M \approx 4$. As can be seen, the highlighted recirculating flow features (inner/outer flow rings that may be used for particle manipulation) are weak for practical applications in the rigid limit. This can be remedied by increasing elasticity (Cau), for which we indeed observe enhanced flow strengths (Fig. 3(b,c)). Finally, we highlight that to obtain a flow topology similar to Fig. 3c, but with a rigid torus, oscillation frequency $\sim 4\times$ higher are necessary (supplementary, section §7), in conformity with the intuition gained via the soft sphere streaming analysis.

5. Conclusion

In summary, this study improves existing three-dimensional rigid sphere streaming theory, expands it to the case of elastic materials, and further corroborates it by means of direct numerical simulations. Our work reveals, in keeping with our previous work on 2D soft cylinders, an additional streaming mode accessible through material compliance and available even in Stokes flow. It further demonstrates how body elasticity strengthens streaming or enables it at significantly lower frequencies relative to rigid bodies. Finally, we show how theoretical insights extend to geometries other than the sphere, highlighting the practical generality of our theory. Overall, these findings advance our fundamental understanding of streaming flows, with potential implications in both biological and engineering domains.

Funding. This work was supported by the NSF CAREER Grant No. CBET-1846752 (MG).

Declaration of Interests. The authors report no conflict of interests.

REFERENCES

- AHMED, DANIEL, MAO, XIAOLE, JULURI, BALA KRISHNA & HUANG, TONY JUN 2009 A fast microfluidic mixer based on acoustically driven sidewall-trapped microbubbles. *Microfluidics and nanofluidics* **7** (5), 727–731.
- ANAND, VISHAL & CHRISTOV, IVAN C 2020 Transient compressible flow in a compliant viscoelastic tube. *Physics of Fluids* **32** (11), 112014.
- BERTELSEN, A, SVARDAL, ASLAK & TJØTTA, SIGVE 1973 Nonlinear streaming effects associated with oscillating cylinders. *Journal of Fluid Mechanics* **59** (3), 493–511.
- BHOSALE, YASHRAJ, PARTHASARATHY, TEJASWIN & GAZZOLA, MATTIA 2020 Shape curvature effects in viscous streaming. *Journal of Fluid Mechanics* **898**, A13.
- BHOSALE, YASHRAJ, PARTHASARATHY, TEJASWIN & GAZZOLA, MATTIA 2021 A remeshed vortex method for mixed rigid/soft body fluid–structure interaction. *Journal of Computational Physics* **444**, 110577.
- BHOSALE, YASHRAJ, PARTHASARATHY, TEJASWIN & GAZZOLA, MATTIA 2022a Soft streaming – flow rectification via elastic boundaries. *Journal of Fluid Mechanics* **945**, R1.
- BHOSALE, YASHRAJ, UPADHYAY, GAURAV, CUI, SONGYUAN, CHAN, FAN KIAT & GAZZOLA, MATTIA 2023 PyAxisymFlow: an open-source software for resolving flow-structure interaction of 3D axisymmetric mixed soft/rigid bodies in viscous flows.
- BHOSALE, YASHRAJ, VISHWANATHAN, GIRIDAR, UPADHYAY, GAURAV, PARTHASARATHY, TEJASWIN, JUAREZ, GABRIEL & GAZZOLA, MATTIA 2022b Multicurvature viscous streaming: Flow topology and particle manipulation. *Proceedings of the National Academy of Sciences* **119** (36), e2120538119.
- BOWER, ALLAN F 2009 *Applied mechanics of solids*. CRC press.
- CHAN, FAN KIAT, BHOSALE, YASHRAJ, PARTHASARATHY, TEJASWIN & GAZZOLA, MATTIA 2022 Three-dimensional geometry and topology effects in viscous streaming. *Journal of Fluid Mechanics* **933**, A53.
- CHEN, YUN & LEE, SUNGYON 2014 Manipulation of biological objects using acoustic bubbles: a review. *Integrative and comparative biology* **54** (6), 959–968.
- CHONG, KWITAE, KELLY, SCOTT D, SMITH, STUART & ELDREDGE, JEFF D 2013 Inertial particle trapping in viscous streaming. *Physics of Fluids* **25** (3), 033602.
- DOU, ZHI, HONG, LIU, LI, ZHENGWEI, CHAN, FAN KIAT, BHOSALE, YASHRAJ, AYDIN, ONUR, JUAREZ, GABRIEL, SAIF, M. TAHER A., CHAMORRO, LEONARDO P. & GAZZOLA, MATTIA 2022 An in vitro living system for flow rectification.
- GAZZOLA, MATTIA, CHATELAIN, PHILIPPE, VAN REES, WIM M & KOUMOUTSAKOS, PETROS 2011 Simulations of single and multiple swimmers with non-divergence free deforming geometries. *Journal of Computational Physics* **230** (19), 7093–7114.
- GAZZOLA, MATTIA, VAN REES, WIM M & KOUMOUTSAKOS, PETROS 2012 C-start: optimal start of larval fish. *Journal of Fluid Mechanics* **698**, 5–18.
- HOLTSMARK, J, JOHNSEN, I, SIKKELAND, TO & SKAVLEM, S 1954 Boundary layer flow near a cylindrical obstacle in an oscillating, incompressible fluid. *The journal of the acoustical society of America* **26** (1), 26–39.
- KAMRIN, KEN & NAVE, JEAN-CHRISTOPHE 2009 An eulerian approach to the simulation of deformable solids: Application to finite-strain elasticity. *arXiv preprint arXiv:0901.3799*.
- KAMRIN, KEN, RYCROFT, CHRIS H & NAVE, JEAN-CHRISTOPHE 2012 Reference map technique for finite-strain elasticity and fluid–solid interaction. *Journal of the Mechanics and Physics of Solids* **60** (11), 1952–1969.
- KLOTSAS, DAPHNE, BALDWIN, KYLE A, HILL, RICHARD JA, BOWLEY, ROGER M & SWIFT, MICHAEL R 2015 Propulsion of a two-sphere swimmer. *Physical review letters* **115** (24), 248102.
- KOTAS, C.W., YODA, M. & ROGERS, P.H. 2007 Visualization of steady streaming near oscillating spheroids. *Experiments in Fluids* **42** (1), 111–121.
- LANE, CA 1955 Acoustical streaming in the vicinity of a sphere. *The Journal of the Acoustical Society of America* **27** (6), 1082–1086.
- LIU, ROBIN H, YANG, JIANING, PINDER, MACIEJ Z, ATHAVALE, MAHESH & GRODZINSKI, PIOTR 2002 Bubble-induced acoustic micromixing. *Lab on a Chip* **2** (3), 151–157.
- LONGUET-HIGGINS, MICHAEL S 1998 Viscous streaming from an oscillating spherical bubble. *Proceedings of the Royal Society of London. Series A: Mathematical, Physical and Engineering Sciences* **454** (1970), 725–742.
- LUTZ, BARRY R, CHEN, JIAN & SCHWARTZ, DANIEL T 2003 Microfluidics without microfabrication. *Proceedings of the National Academy of Sciences* **100** (8), 4395–4398.

- LUTZ, BARRY R, CHEN, JIAN & SCHWARTZ, DANIEL T 2005 Microscopic steady streaming eddies created around short cylinders in a channel: Flow visualization and stokes layer scaling. *Physics of Fluids* **17** (2), 023601.
- LUTZ, BARRY R, CHEN, JIAN & SCHWARTZ, DANIEL T 2006 Hydrodynamic tweezers: 1. noncontact trapping of single cells using steady streaming microeddies. *Analytical chemistry* **78** (15), 5429–5435.
- MARMOTTANT, PHILIPPE & HILGENFELDT, SASCHA 2003 Controlled vesicle deformation and lysis by single oscillating bubbles. *Nature* **423** (6936), 153–156.
- MARMOTTANT, PHILIPPE & HILGENFELDT, SASCHA 2004 A bubble-driven microfluidic transport element for bioengineering. *Proceedings of the National Academy of Sciences* **101** (26), 9523–9527.
- PANDE, SHRIHARI D, WANG, XIAOJIA & CHRISTOV, IVAN C 2023 Oscillatory flows in compliant conduits at arbitrary womersley number. *arXiv preprint arXiv:2304.00543* .
- PARTHASARATHY, TEJASWIN, BHOSALE, YASHRAJ & GAZZOLA, MATTIA 2022 Elastic solid dynamics in a coupled oscillatory couette flow system. *Journal of Fluid Mechanics* **946**, A15.
- PARTHASARATHY, TEJASWIN, CHAN, FAN KIAT & GAZZOLA, MATTIA 2019 Streaming-enhanced flow-mediated transport. *Journal of Fluid Mechanics* **878**, 647–662.
- POMMELLA, ANGELO, HARUN, IRINA, HELLGARDT, KLAUS & GARBIN, VALERIA 2021 Enhancing microalgal cell wall permeability by microbubble streaming flow. *arXiv preprint arXiv:2112.08519* .
- SPELMAN, TAMSIN A & LAUGA, ERIC 2017 Arbitrary axisymmetric steady streaming: Flow, force and propulsion. *Journal of Engineering Mathematics* **105** (1), 31–65.
- THAMEEM, RAQEEB, RALLABANDI, BHARGAV & HILGENFELDT, SASCHA 2017 Fast inertial particle manipulation in oscillating flows. *Physical Review Fluids* **2** (5), 052001.
- WANG, CHENG, JALIKOP, SHREYAS V & HILGENFELDT, SASCHA 2011 Size-sensitive sorting of microparticles through control of flow geometry. *Applied Physics Letters* **99** (3), 034101.
- WANG, CHANG-YI 1965 The flow field induced by an oscillating sphere. *Journal of Sound and Vibration* **2** (3), 257–269.